Modeling amorphous $Si_3B_3N_7$: Structure and elastic properties

A. Hannemann, J. C. Schön, and M. Jansen
Max-Planck-Institut für Festkörperforschung, Heisenbergstr. 1, D-70569 Stuttgart, Germany

H. Putz
Crystal Impact GbR, 53002 Bonn, Germany

T. Lengauer
Max-Planck-Institut für Informatik, 66123 Saarbrücken, Germany

(Received 2 September 2003; revised manuscript received 25 February 2004; published 5 October 2004)

We investigate the structure and elastic properties of the amorphous high-temperature ceramic *a*-$Si_3B_3N_7$. Several different structural models are generated and their properties such as the radial and angular distribution functions, the degree of local order, the density, the bulk modulus and the phonon spectrum, are calculated and compared with the experiment. The best structural agreement between model and experimental observations is found for models exhibiting a certain degree of local (<1 nm) heterogeneity in the cation distribution. We show that this is consistent with the fact that *a*-$Si_3B_3N_7$ has not been synthesized by cooling from the melt but via the polymerization and subsequent pyrolysis of molecular precursors. Furthermore, we suggest that, due to the synthesis process, stable nanoscale cavities ($\oslash < 1$ nm) will be formed that result in the compound's relatively low density ($\approx 1.8-1.9$ g/cm^3).

DOI: 10.1103/PhysRevB.70.144201 PACS number(s): 81.05.Je, 81.05.Kf, 61.43.−j, 61.43.Fs

I. INTRODUCTION

One of the most fascinating new classes of materials for high-temperature applications have been the multinary nitrides and carbides such as *a*-$Si_3B_3N_7$ or *a*-$SiBN_3C$,[1–3] which exhibit amazing mechanical and thermal stabilities in spite of their amorphous structure. For example, *a*-$Si_3B_3N_7$ is stable up to $T_{dec} \approx 1900$ K when decomposition sets in, without any crystallization taking place.[2] Even more stable is *a*-$SiBN_3C$ ($T_{dec} \approx 2100$ K), which is also highly stable in oxygen atmosphere up to $T \approx 1700$ K.[2] In general, the elastic constants of these materials are rather high[2] (e.g., the bulk modulus of *a*-$SiBN_3C$ is $B = 200-300$ GPa); in spite of their low density of about 1.9 g/cm^3, they exhibit a high breaking strength.

Since the ceramics are amorphous, the starting point for an investigation of these materials must be the generation of appropriate microscopic structural models. In this work, we are going to focus on the prototypical ternary nitride *a*-$Si_3B_3N_7$, since its composition is well-defined, in contrast to, e.g., *a*-$SiBN_3C$, where a greater spread in composition is found. One major problem when trying to model these nitridic ceramics is the complicated synthesis route: First, precursor molecules such as TADB $[(Cl_3Si)\text{-}(NH)\text{-}(BCl_2)]$ form oligomers via HCl-elimination in NH_3, followed by a pyrolysis in N_2 atmosphere,[1] where, depending on the details of the synthesis (choice of precursor, atmosphere, and temperature schedule during pyrolysis, etc.), different precursor-derived ceramics are produced. Trying to reproduce these processes in a simulation is nearly impossible, and thus we have explored a number of different computational methods to generate a variety of structural models that might approximate the final ceramic sufficiently well. Each of these procedures connects to a particular commonly used experimental approach for the generation of amorphous materials.

In earlier preliminary work[4] we have presented several such model structures, some of which satisfactorily reproduce the physical structural measurements. According to these studies, it appears that *a*-$Si_3B_3N_7$ is a dense "covalent" network, consisting of a homogeneous distribution of SiN_4-tetrahedra and trigonally planar BN_3-units. Experiments such as NMR- and EXAFS-studies have demonstrated that this local coordination is in agreement with experiment.[5] Interestingly, the "best"—with respect to agreement between computed and experimental radial distribution functions—models consisted of sintered nanoscale crystal fragments exhibiting a heterogeneity in the Si/B-distribution on length scales of $\approx 1/2$ nm.[4] This also appears to be consistent with experiment: TEM-studies have shown that down to ≈ 1 nm the Si/B-distribution is homogeneous,[6] while the analysis of NMR-REDOR-data has recently yielded clear evidence for a certain degree of heterogeneity on length scales up to a few Å.[7,8]

In this paper, we are going to present in detail five different classes of structural models based on different generation procedures, each associated with a different chemical and physical route that might, in principle, allow us to generate *a*-$Si_3B_3N_7$. First, we describe and shortly discuss the various techniques. Next, the resulting structural models are compared among each other and with geometrical and topological information gained from physical measurements. Finally, several physical properties such as the bulk modulus and the phonon spectra will be calculated, and compared with experimental data as far as available (Table I).

II. MODEL GENERATION

In general, each of our modeling approaches can be divided into two steps. The first, major one, consists of the

TABLE I. Overview of model classes (A–E) and modeling procedures P (1–10). Details of the modeling procedures are given in Table II.

Class	P	Explanation
	1	Melt equilibrated with molecular dynamics (MD) followed by cooling with MD
A	2	Melt equilibrated with MC followed by cooling with MC
	3	Melt equilibrated with MD followed by global optimization with simulated annealing
	4	Simulated annealing of low density crystal fragment
B	5	Constant pressure Monte Carlo cooling of medium density crystal fragment
	6	Constant volume Monte Carlo cooling of medium density crystal fragment
C	7	Constant pressure Monte Carlo cooling of cluster with open boundary conditions
	8	Constant pressure Monte Carlo cooling of periodically repeated interior of cluster
D	9	Random close packing model
E	10	Sol-gel model

generation of the "raw" model, where the final network topology is established to over 90%. Depending on the synthesis class, several techniques, including possibly a global optimization, might be needed. In each instance, this first stage is followed by a local (conjugate gradient) relaxation and fine-tuning of the "raw" model structures based on refined potentials and cost functions described in Sec. II B.

A. Classes of model generation

1. Cooling from the melt (class A)

The procedure to generate a model for a-$Si_3B_3N_7$ via rapid cooling from the melt started by heating a hypothetical crystalline structure of $Si_3B_3N_7$ (Ref. 9) in a periodically repeated cubic box with side length $L=19.1$ Å to 2500 K followed by an equilibration for 1.0 ns, using the (N,V,T)-ensemble [(N,V,T)- and (N,p,T)-ensemble refer to simulations with constant particle number, volume, and temperature, and constant particle number, pressure and temperature, respectively] molecular dynamics (MD). The size of the system was $N_{\text{atom}}=N_{\text{Si}}+N_{\text{B}}+N_{\text{N}}=702$ atoms, with $N_{\text{Si}}=162$, $N_{\text{B}}=162$, and $N_{\text{N}}=378$. For the MD-simulations, we employed a velocity-Verlet integration algorithm,[10] with a time step $\Delta t=1.0$ fs. The temperature was fixed by periodic velocity rescaling, and we used a computationally efficient empirical two-body potential A (Ref. 11) to describe the potential energy of the system. Next, the system was rapidly cooled down to 0 K using molecular dynamics simulated annealing with three cooling rates $\gamma^{\text{MD}}=2.5\cdot10^{12}$, $2.5\cdot10^{11}$, $2.5\cdot10^{10}$ K/s while keeping the volume constant. This cooling was performed for three different starting configurations taken along the 1 ns trajectory at 2500 K. As an alternative, we also performed slow cooling via Monte Carlo (MC) simulated annealing for the same system. First, the system was equilibrated at $T=2500$ K for 10^6 MCC. We then employed several cooling rates $\gamma^{\text{MC}}=2.5\cdot10^{-1}$, $2.5\cdot10^{-2}$, $2.5\cdot10^{-3}$ K/MCC again keeping the volume constant, starting at three different melt configurations. The moveclass of the MC simulations consisted of single atom moves, where the atom chosen was shifted by a random vector $\boldsymbol{d}$. The stepsize $|\boldsymbol{d}|$ was adjusted such that for each temperature an acceptance rate of about 50% was achieved. Each Monte Carlo cycle (MCC) consisted of a random sweep over all atoms in the system, i.e., N_{atom} individual atom moves.

In addition, we used stochastic simulated annealing as a global optimization (GO) procedure by performing the annealing from a number of high-temperature starting points, i.e., we heated the equilibrated ($T=2500$ K) melt to initial temperatures $T_0=5000$ and 6000 K. Again, three different cooling rates $\gamma=30,3,0.3$ K/MCC were used for each T_0.

For comparison, we also performed local optimizations as described in Sec. II B for each of the equilibrated high-temperature configurations, corresponding to quenches with infinite cooling rates.

2. Sintering of crystal fragments (class B)

An alternative route to a-$Si_3B_3N_7$ might be the solid state sintering of microcrystallites of BN and Si_3N_4. However, so far, such experiments do not appear to lead to a ternary Si/B/N compound. It seems that there does not exist a sufficiently strong driving force that would lead to a mixing, once we are below the melting point, of the two binary end-compounds. [*Ab initio* energy calculations (Ref. 9) and calculations with the empirical potentials used in this work (Ref. 12), both suggest that at zero temperature a phase separation into crystalline BN and Si_3N_4 should be preferred to hypothetical crystalline (or amorphous) ternary $Si_3B_3N_7$ compounds.] However, these purely equilibrium considerations do not exclude the possibility that sintering of nanometer-sized crystallites could lead to a kinetically stable amorphous ternary phase. Thus, we have constructed a model[4] for a-$Si_3B_3N_7$ that consists of many ($\approx$15) BN and Si_3N_4 nanocrystallites ($\oslash<1/2$ nm). The system consisted of $N_{\text{atom}}=1144$ atoms, with $N_{\text{Si}}=264$, $N_{\text{B}}=264$, and $N_{\text{N}}=616$, in a periodically repeated cubic box of side-length $L=27$ Å, resulting in an initial density of $\rho=1.5$ g/cm^3. Besides the standard energy relaxation and fine tuning as described in Sec. II B, we have also performed global optimizations using stochastic simulated annealing ($T_0=3,4,5\times10^3$ K and three cooling rates $\gamma=30,3,0.3$ K/MCC each), where the volume was kept constant. Again, potential A was used for the energy evaluation.

For comparison, we performed additional global and local optimizations at higher initial density $\rho=2.01$ g/cm^3, rescaling the side length for this purpose to $L=25.03$ Å, where we performed two sets of global optimizations, keeping the volume and the pressure constant, respectively. Again several starting temperatures ($T_0=1,2,\ldots,5\times10^3$ K) and three cooling rates ($\gamma=10^{-1},10^{-2},10^{-3}$ K/MCC) were used.

We note that a second reason to investigate a nanocrystallite model is that phase separation on the nanometer scale might well occur in the course of any synthesis route for a-

$Si_3B_3N_7$. Since the time scales involved in such phase separation processes are too large for straightforward MD/MC simulations, one has to study the effects by introducing such phase separated regions by hand. Clearly, this crystal fragment model is expected to exaggerate the heterogeneity of the cation distribution by assuming fully formed nanocrystallites. Nevertheless, it constitutes a possible structure model that takes some features of, e.g., the melt-route structure generation process into account that would otherwise not be accessible. Furthermore, it constitutes a limiting case for those structure models that incorporate inhomogeneities of the cation distribution.

3. Molecular modeling (class C)

A traditionally quite popular way to generate computer models for amorphous systems has been the molecular modeling approach.[13] Starting with a small nucleus consisting of a few atoms, one builds the amorphous structure in an atom-by-atom or building-block-by-building-block fashion, taking some local coordination information into account. Typically, this procedure results in a cluster, since periodic boundary conditions are not easily accommodated in the generation process.

Physically, this process would correspond to the slow growth of one (or many) cluster in vacuum, where small precursor molecules or individual atoms are adsorbed on the surface, followed by chemical reactions and, possibly, a reorganization of the cluster or part of it, in order to relieve tensions. As a final step, such clusters might be deposited on a surface and allowed to sinter yielding an amorphous film.

Clearly, a comparison of such a cluster with bulk amorphous compounds is difficult as long as surface effects are relevant. Since sufficiently large amorphous network clusters containing hundreds of thousands of atoms are not easily constructed, we have generated a periodic model using molecular modeling via a two-step process.

First, we generate clusters using the molecular modeling procedure originally developed by Gladden,[14] and refined by Wefing.[15] Starting from a few-atom nucleus, we add atoms, alternating between nitrogen and the cations (B and Si being chosen at random, with $N_{Si}:N_B \approx 1$ on average), while requiring that the local coordinations [BN_3-triangles, SiN_4-tetrahedra, and $N(Si,B)_3$-triangles] and geometric constraints are fulfilled. Once this is no longer possible, we allow some removal of recently added atoms, in order to attempt a new line of construction. As the cluster grows, further improvements become increasingly more difficult, until the time needed to add further atoms (including the deconstruction and rebuilding time of the cluster) exceeds all practical limits. For the Si/B/N clusters we have constructed, this typically takes place when the cluster reaches a size of a thousand atoms.

In a second step, we cut a cubic section from the interior, containing about 600 atoms, and use this as the periodically repeated simulation cell for the relaxation calculations. Since this results in energetically unfavorable interfaces at the boundaries of the simulation cell, careful annealing starting at relatively high temperatures is needed to reach a reasonable structure. The system was allowed to equilibrate at two initial temperatures $T_0=1500$ and 2500 K using Monte Carlo simulations at constant pressure. For three end-configurations from different random walk trajectories, we performed the usual local optimizations (cf. Sec. II B). Furthermore, these configurations served as starting points for slow coolings with two different initial temperatures ($T_0=1500$ and 2500 K) and cooling rates ($\gamma=2.5\times10^{-1}$, 2.5×10^{-2}, 2.5×10^{-3} K/MCC).

For comparison, the same annealing procedure was performed for the original cluster without periodic boundary conditions. The structural properties of the periodic structures could then be compared with those one would find for the interior of the original cluster.

4. Random close packing (class D)

Chemical vapor deposition of molecules containing (Si-N)-, (B-N)-, or (Si-N-B)-units, or atom beam deposition of the participating atoms Si, B, and N, on a substrate followed by low-temperature sintering would be another possible route to generate bulk amorphous Si/B/N-materials, in this instance, as an amorphous film. The presintering structure generated in this way would be a random arrangement of Si and B atoms probably already surrounded by (and bonded to) nitrogen. One possible model describing the structures produced in this way is the so-called random close packing (RCP) model adapted for the generation of covalent networks.[16] Here, one generates a random close packing of the anions, followed by a random distribution of the cations over the voids in the anion packing, and finally allows the structure to relax. We generated five different topologies using this procedure, each containing 1040 atoms.

5. Sol-gel route (class E)

While constituting reasonable structures, none of the preceding models has been generated in a fashion that corresponds to the route chosen by the experimental chemist. As mentioned above, a true simulation of the full sol-gel route is not yet feasible. Nevertheless, we have developed a multistage separation of time scales approach[17] to model the polymerization and pyrolysis steps involved, and which allows us to investigate the effects of the kinetics of the polymerization, that appears to favor the early formation of B-N bonds.

In this method, about 1% of the $N_{atom}=N_{Si}+N_B+N_N$ atoms (typically $N_{atom}\approx1300$) were placed onto a diamond-type lattice in a periodically repeated simulation cell to serve as aggregation initiation sites. Additional atoms were placed on open lattice points next to the atoms already on the lattice, with the correct local bonding environment, i.e., only up to four and three neighbors are allowed for Si, and B and N, respectively, and similarly no cation-cation or anion-anion nearest neighbors were permitted. The kinetic effect was taken into account by giving a preference $p^0_{(N\text{-}B)}$ to B-atoms whenever it was a N-atom's turn to choose a new neighbor, while ensuring that the final composition was as desired ($N_{Si}=N_B$). The cell volume was chosen such that a density of $\rho^{init}=1.53\ g/cm^3$ was achieved, which is consistent with the density at the beginning of the pyrolysis stage of the actual

TABLE II. Details of the modeling procedures. P is the number of the procedure. N_{atom} is the number of atoms employed. The initial densities ρ_0 are given in g/cm^3, and the initial temperatures T_0 are in K. The models were kept for t_{eq} time steps at the initial temperature T_0, before the global optimization/slow cooling began. The cooling rates γ are given in K/MCC and K/s for the MC and MD simulations, respectively. Similarly, the equilibration times t_{eq} are given in MCC and fs for MC and MD-simulations, respectively. Ens denotes the ensemble in which the global optimizations/coolings were performed. In the *NpT* ensemble, the external pressure was set to zero. Three trajectories for each set of the optimization parameters T_0, t_{eq}, and γ were generated. N_{mod} is the total number of raw models generated for the specific modeling procedure.

Class	P	N_{atom}	ρ_0	T_0	t_{eq}	γ	Ens	N_{mod}
A	1	702	2.75	2500	10^6	$2.5\cdot(10^{12},10^{11},10^{10})$	*NVT*	9
	2	702	2.75	2500	10^6	$2.5\cdot(10^{-1},10^{-2},10^{-3})$	*NVT*	9
	3	702	2.75	5000, 6000, 7000	10^3	$3.0\cdot(10^{1},10^{0})$	*NVT*	18
B	4	1144	1.54	5000, 6000, 7000	10^3	$3.0\cdot(10^{1},10^{0},10^{-1})$	*NVT*	27
	5	1144	2.01	1000, 2000, 3000	10^5	$1.0\cdot(10^{-1},10^{-2},10^{-3})$	*NpT*	36
	6	1144	2.01	1000, 2000, 3000	10^5	$1.0\cdot(10^{-1},10^{-2},10^{-3})$	*NVT*	36
C	7	974	2.65	1500, 2500	10^6	$2.5\cdot(10^{-1},10^{-2},10^{-3})$	*NpT*	18
	8	562	2.85	1500, 2500	10^6	$2.5\cdot(10^{-1},10^{-2},10^{-3})$	*NpT*	18
D	9	1040	2.83	n.a.	n.a.	n.a.	n.a.	5
E	10	1300	1.57	1000, 2000, 3000	10^6	n.a.	*NpT*	30

synthesis ($\rho=1-1.4$ g/cm^3).[18] Using this procedure, we generated five structures each for three numbers of aggregation sites (3, 15, and 30) and two choices for the initial bonding probabilities $p^0_{(N\text{-}B)}=0.95$ and $p^0_{(N\text{-}B)}=0.99$. Before the local optimization according to Sec. II B, these structures were tempered for 10^6 MCC for a range of temperatures $T_0=1000$, 2000, and 3000 K.

B. Local relaxation and structure refinement

Although at the end of each generation procedure the resulting structure already possessed the final network topology, several of these "raw" models, e.g., the models produced by the RCP procedure or the crystal-fragment based models, still exhibited a locally distorted structure. Thus, we performed in each case additional local optimizations of the energy using the conjugate gradient technique. Two different potentials have been employed to calculate the potential energy, potential A,[11] which contained only two-body terms without Coulomb contributions, and a more complex potential B,[19] that included two- and three-body as well as Coulomb terms. (Since the functional form of these potentials is rather complicated, we refer to the literature[11,19] for more details.) For comparison purposes, two different strategies were used for each interaction potential [resulting in four procedures labeled I (potential A/Opt 1), II (A/2), III (B/1), and IV (B/2), respectively]:

(1) We proceed in two steps: First, we optimize the atom positions while keeping the simulation cell fixed (constant volume optimization), in order to remove the most egregious tensions from the system. Next, we optimize both atom positions and cell variables (constant pressure optimizations).

(2) We vary atom position and cell variables concurrently to find the nearest local minimum.

We note that both potentials have been fitted to reproduce the structure and phonon spectrum of the binary end-compounds BN and Si_3N_4, and the structures of hypothetical ternary crystalline $Si_3B_3N_7$ compounds that had been optimized using *ab initio* methods. Furthermore, the potentials reproduce the *ab initio* calculations of simple molecules containing Si, B, and N.

After the local optimizations, our final step consisted of a reverse Monte Carlo (RMC) type stochastic quench at constant volume. The cost function $C(\mathbf{r}_i;\lambda)$ was given as a linear combination of the difference between the computed and experimentally measured (via x-ray or neutron scattering) radial distribution function $(\Delta R_B(\mathbf{r}_i))^2$, and the potential energy, $C(\mathbf{r}_i;\lambda)=\lambda(\Delta R_B(\mathbf{r}_i))^2+(1-\lambda)E^A_{pot}(\mathbf{r}_i)$. We chose $\lambda=0.20$ and the structures were optimized for 5×10^5 MCC. Typically, the changes in the atom positions in this final refinement step were small (<0.03 Å/atom).

C. Summary of the model generation

Using the five different general approaches described above, about 200 structure models have been generated, using ten particular modeling procedures: Each of these procedures contained several parameters, and each was followed by four local optimizations procedures as described in Sec. II B. The only exception was the open cluster, where constant volume minimizations did not apply, and the sol-gel process, where we always performed the second group of minimizations (constant volume followed by constant pressure). In addition, for all procedures that involved a global optimization or cooling stage we also performed these local optimizations (quenches) directly for the starting configurations of the annealing procedure, for comparison. Table II gives an overview over all the models, listing the total number of atoms involved, what kind of cooling/global optimization procedure (if any) was applied, and what specific parameters of the annealing were varied.

TABLE III. Summary of available experimental data for *a*-$Si_3B_3N_7$, regarding first (a) (Refs. 5 and 20) and second (b) (Ref. 7) coordination spheres, respectively. The mean distances $\overline{d}$ are given in Å.

(a) Pair	$\overline{d}$	CN	Local geometry
B-N	1.43	2.8–3.0	trig. planar
Si-N	1.72	3.4–3.8	tetrahedr.
N-B	1.43	1.2–1.4	trig. planar
N-Si	1.72	1.4–1.6	trig. planar
N-(Si/B)	n.a.	2.6–3.0	trig. planar
(b) B-B	B-Si	Si-B	Si-Si
4(-5)	1.3–1.5	1.7–1.9	6
ρ_{exp}		1.9 g/cm^3	

III. STRUCTURAL PROPERTIES

For each of the ten modeling procedures belonging to the five classes of structure models for *a*-$Si_3B_3N_7$, we have analyzed various structural properties: the radial pair correlation and angular distribution functions, the mean coordination numbers within the first and second neighbor spheres around the atoms, and the ring statistics. (The ring sizes were determined from the shortest paths emanating from a nearest neighbor atom of a central atom to a different nearest neighbor atom of that central atom.) Experimentally, direct comparisons are possible for the radial distribution function measured with x-ray and neutron scattering, for the first coordination sphere via, e.g., EXAFS or NMR measurements, and for the second coordination sphere via the analysis of REDOR-NMR experiments. Angular distributions are only accessible in an indirect fashion, and the same holds true for, e.g., the third neighbor sphere. Finally, fingerprinting of IR/Raman data can possibly give access to information regarding the presence of various ring structures in the amorphous network. The available experimental data are summarized in Table III. Structural properties of models that represent the *different* classes are given in Sec. III A, while in Sec. III B, the dependence of the properties of the models within each class on the specific choice of the simulation parameters are discussed.

A. Comparison of classes

In order to compare the structural properties of models that are typical for each class, we show the data for those models that were optimized using the local optimization procedure IV (*NpT*-minimization with potential B). First we discuss the pair correlation functions, next we focus on the first coordination spheres and finally discuss the second coordination spheres and the ring statistics.

1. Pair correlation functions

Figure 1 shows a comparison of the x-ray and neutron pair correlation function $D_{N/X}(R)$ of the models, representing the different classes, and the experimental data, after the energy minimization and after the final RMC-fine-tuning, respectively. The models agree with the general shape of the experimental function, and the various peaks can be associated with specific atom-atom distances within the first and second neighbor spheres: 1.43 Å with B-N bond distances, 1.72 Å with Si-N bond distances, 2.44 Å with B-N-B and N-B-N distances, 2.74 Å with N-Si-N and Si-N-B distances and the shoulder at about 3.1 Å with Si-N-Si distances, respectively. The best quantitative agreement is found for the crystal fragment (class B) and the sol-gel model (class E) (cf. Table IV). We also note the fact that even after the RMC-fine tuning there exist noticeable differences between the various models, which are greater than the spread within a given class (cf. Table V).

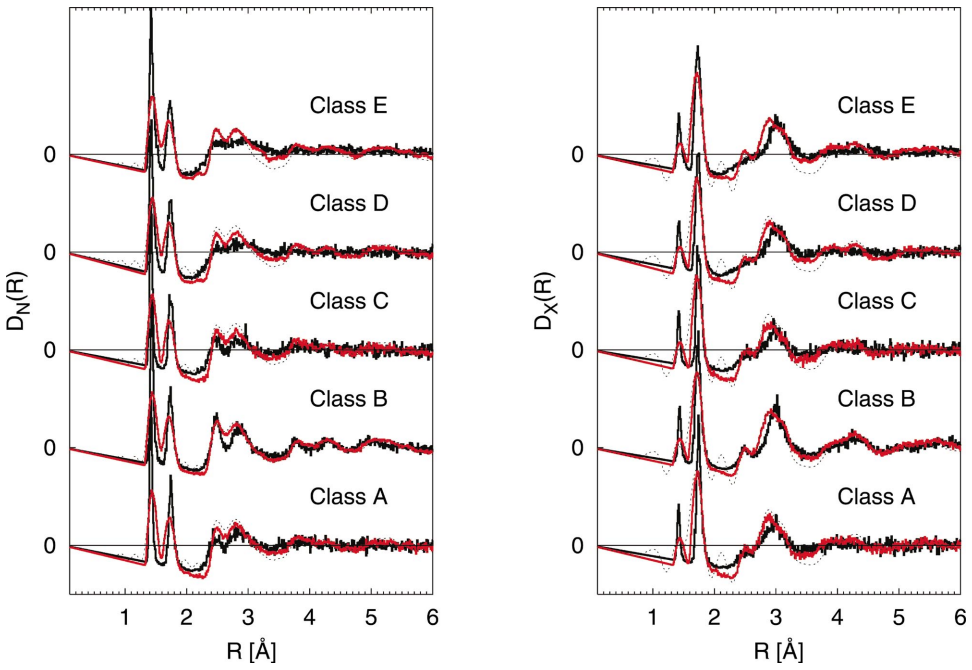

FIG. 1. (Color) Neutron (left) and x-ray (right) diffraction pair correlation $D_{N/X}(R)$ for the models of the classes A–E, after thermal treatment and after local optimizations. The red curves are the pair correlation functions after the RMC-refinement, the full black lines show the pair correlation functions after the local optimizations and the dashed curves are the experimental pair correlation functions. The distances *R* are given in Å. The differences of intensities of the peaks are due to the different scattering factors of the pairs of atoms, that contribute to that peak.

TABLE IV. Peak positions in the experimental pair correlation functions of a-$Si_3B_3N_7$ and the corresponding atom-atom distances, that are determined in this work. All distances are given in Å. We have added roman numerals to those pairs that contribute to more than one peak in the experimental pair correlation function.

Peak	Pairs/distances
1.43	B-N(I) 1.43
1.72	Si-N(I) 1.72
2.50	N-N(I) 2.50, B-B(I) 2.50
2.77	N-N(II) 2.71, Si-B(I) 2.75
3.00	B-N(II) 2.90, Si-Si(I) 3.0
3.80	B-N(III) 3.80
4.20	Si-N(II) 4.20, B-B (IV) 4.25
5.20	N-N(III) 5.2, B-B(V) 5.0

From the partial pair correlation functions $D^{AB}_{N/X}(R)$ for neutron (N) and x-ray (X) scattering experiments we can associate additional peaks between about 3.8 and 4.2 Å in the experimental pair correlation function with third neighbor Si-N and B-N distances, and the oscillations at about 4.5–5 Å with fourth neighbor N-N and Si-N distances (cf. Table IV). There also exist small peaks in the B-B, Si-B, Si-Si, and N-N partial pair correlation functions at about 2.05, 2.2, and 2.6 Å, which indicate the existence of edge sharing polyhedra in the structural models. The differences in the models belonging to different classes can be most easily seen in the intensities of the peaks associated with (second coordination sphere) B-B, Si-B and the Si-Si partial pair correlation functions: The models of classes A, C, and D contain more Si-B and less B-B and Si-Si next-nearest neighbor pairs than the models of classes B and E.

TABLE V. Comparison of the different properties that distinguish between the different models. The internal spread in the pair correlation function $\Delta D^Y(R)$ of a class Y containing n_Y models is $\Delta_{YY}(D(R)) = (1/N_R)\Sigma_{i=1}^{N_R}\Sigma_{m=1}^{n_Y}[D^m(R_i) - \overline{D^Y(R_i)}]^2$, where $\overline{D^Y(R_i)} = (1/n_Y)\Sigma_{m=1}^{n_Y} D^m(R_i)$ is the average value of the pair correlation function at distance R_i and $D^m(R_i)$ is the value of the pair correlation function at R_i in model m belonging to class Y. N_R is the number of distances R_i included. To compare the pair correlation functions of models belonging to *different* classes Y and Z, we calculate $\Delta_{YZ}(D(R)) = (1/N_R)\Sigma_{i=1}^{N_R}[\overline{D^Y(R_i)} - \overline{D^Z(R_i)}]^2$, where $\overline{D^Y(R_i)}$ and $\overline{D^Z(R_i)}$ are the average pair correlation functions of models belonging to classes Y and Z, respectively. (a) Densities in g/cm^3 and coordination numbers of the second coordination spheres. (b) Spread in the neutron pair correlation functions $\Delta_{YY}D_N(R)$ and $\Delta_{YZ}D_N(R)$.

(a)	ρ	CN2(Si-Si)	CN2(B-B)		
A	2.85±0.02	3.70±0.10	2.30±0.15		
B	2.30±0.05	5.71±0.04	4.66±0.06		
C	2.74±0.02	4.26±0.08	3.35±0.09		
D	2.78±0.05	4.25±0.10	3.23±0.14		
E	1.90±0.10	4.33±0.09	4.09±0.07		
(b)	A	B	C	D	E
A	0.15	0.38	0.32	0.17	0.93
B	0.38	0.09	0.44	0.30	0.60
C	0.32	0.44	0.20	0.25	0.81
D	0.17	0.30	0.25	0.18	0.71
E	0.93	0.60	0.81	0.71	0.13

2. Local coordinations and angular distribution functions

Considering the mean coordination numbers (MCN) and the distribution of the coordination spheres of silicon, boron and nitrogen of the refined models, we find that silicon atoms are mainly fourfold coordinated (MCN=3.7–4.0), whereas boron atoms are surrounded by three nitrogen atoms (3.0–3.1), and nitrogen is surrounded mostly by three cations (2.9–3.0). Comparing the silicon and boron atoms, we find that boron atoms achieve their ideal coordination number more often than the silicon atoms, and that coordination defects will be more frequently found at silicon than at boron. Differences between the models belonging to different classes can be found in the distribution of the nitrogen coordination spheres NSi_xB_{3-x}. For models derived from the classes A, C, and D, the distribution of NSi_xB_{3-x} shows a preference for NSi_2B_1 and NSi_1B_2 coordination spheres, while the models of classes B and E contain a higher percentage of NSi_3 and NB_3 coordination spheres.

Regarding the angular distribution functions for the N-B-N, the N-Si-N and (B/Si)-N-(B/Si) angles, all models clearly show that the dominant angles at Si, B, and N are those that correspond to a tetrahedral and trigonal coordination, respectively. In addition, all models exhibit a small peak at 90° in the N-Si-N and N-B-N distributions. This agrees with the observation in Sec. III A 3 below, that a certain number of edge connected SiN_4-tetrahedra and BN_3-triangles are present in all these models. The interatomic distances d_{90}(X-Y), with X, Y=Si or B, corresponding to these 90° angles are $d_{90}(B\text{-}B) \approx 2.02$ Å, $d_{90}(Si\text{-}B) \approx 2.23$ Å and $d_{90}(Si\text{-}Si) \approx 2.44$ Å. Since these values are close to other relevant interatomic distances, they will at most result in small shoulders of large peaks in the total pair correlation functions.

3. Second coordination spheres and ring statistics

Even though all models yielded similar values for the first coordination sphere and similar results for the angular distribution functions, the second (cation-cation) coordination spheres demonstrate the differences between the classes. The models corresponding to classes B and E contain more Si-Si (5.7, 4.4) and, in particular, B-B next-nearest neighbor (4.0, 3.7) contacts than the other models (3.8-4.2 for Si-Si and 2.0-2.8 for B-B, respectively), thus being in best agreement with experiment.

There exist about 5–7% 4-rings in the models generated in classes A–C and about 10–12% in classes D and E, respectively. The 4-rings are associated with the small peaks at about 90° in the angular distribution functions and the small prepeaks in the partial pair correlation functions. No preference for edge-sharing between two SiN_4-tetrahedra over edge-sharing between a SiN_4 tetrahedron and a BN_3 triangle

can be observed in the distribution of the compositions of four-member rings. The highest fraction of six-member rings (40%) is found in the crystal fragment-based models that initially contain a considerable number of borazene rings (B_3N_3), compared with $\approx 20-25\%$ for classes A, C, D, and 30% for class E. The models of class B contain about 40% B_3N_3 and Si_3N_3 rings each among the 6-rings, clearly showing that a considerable part of the initial structure has remained intact. In contrast, models of the classes A, C, and D exhibit mostly mixed cation 6-rings; only class E models show an enhanced amount of borazene rings.

B. Comparison of classes and procedures

In the previous subsections, we have presented and compared the results for typical models of each class for the optimized and the refined models. Now we are going to focus on each class separately, and analyze the different procedures involved. We have to address four different aspects: influence of specific modeling parameters (if present), parameters of the global optimization (if performed), effect of the two potentials used for the refinement and energy relaxation, and the effect of performing only a constant pressure local minimization vs a combination of constant volume followed by constant pressure minimization. We present our results for the models determined from the local optimizations only, since the RMC-refinement procedure does not change the structural properties significantly.

We have found that the effect of the choice of potential for the final local optimizations is the same for all procedures, and does not correlate with the other choices of optimization parameters or influence the comparison between two procedures, except for those procedures, that employed very fast cooling. Thus, the various trends being the same for potential A and potential B, all the comparison data we show below are for calculations with the more complex potential B.

Regarding the question of performing only one constant pressure minimization or a combination of constant volume followed by constant pressure minimization, we found that the effect is most pronounced for those procedures where neither a global optimization nor a slow cooling stage had been included. In these latter cases, we find that only performing constant pressure minimizations right away led to somewhat higher densities than first allowing the system to remove extreme tensions by constant volume minimizations.

For the RCP model, we are not going to present a specific analysis, since a detailed study of the influence of the various parameters involved for the RCP model has already been given[16] for several example systems such as a-SiO_2, a-Si_3N_4, and amorphous Si/O/N. Similarly, for the sol-gel model, a detailed analysis of the many model parameters and possible sub-models that can be constructed within the context of the sol-gel model has been presented in Ref. 17.

1. Class A: Cooling-from-melt models

The comparison of the pair correlation functions of the MC and MD cooling using comparable cooling rates shows no difference between these methods. We again find the peaks at 1.43 Å and 1.72 Å resembling B-N and Si-N interatomic distances. Both these peaks are slightly wider for faster cooling. Furthermore, within each procedure, slower cooling leads to more pronounced peaks at about 2.4 and 2.74 Å. The pair correlation functions are rather featureless for distances larger than 3.5 Å. Finally, quenching the (at 2500 K) equilibrated models, leads to pair correlation functions that are similar to the one calculated for models that were rapidly cooled and locally optimized.

Each of the three procedures was performed for three different cooling rates, with the global optimization simulated annealing, in addition, starting from three very high initial temperatures. Fast cooling leads to stronger deviations from the ideal coordination numbers three and four for boron and silicon, respectively. Additionally, we find for the MC and MD cooling procedures, that higher cooling rates lead to the existence of a higher fraction of four-member rings. Finally, no clear dependence of the mean coordination numbers of second coordination spheres on either T_0 or γ can be deduced from our data.

2. Class B: Crystal fragment models

The models obtained from a slow cooling process that started after the system had been "equilibrated" at a low temperature ($T_0 = 1000$ K), exhibit a well-structured pair correlation function. These pair correlation functions contain all peaks up to about 5 Å, that have already been discussed in Sec. III A and summarized in Table IV. However, keeping the system at 3000 K prior to cooling leads to significant differences in the pair correlation functions of the models, obtained after cooling. For the *NpT*-simulations, the pair correlation functions are featureless at distances $R > 3.5$ Å for the two slowest cooling rates, if the system was equilibrated at 2000 K, and for all cooling rates, if the system was kept at 3000 K prior to cooling. In the *NVT*-simulations, the lack of features at distances $R > 3.5$ Å can be found for the initial temperature $T_0 = 3000$ K. For the global optimizations, we find similar results. Heating the system to 5000 K or 6000 K followed by rapid cooling still results in well-structured pair correlation functions.

This feature, i.e., that models that have spent a considerable amount of time at temperatures $T \geqslant 2000$ K result in structures partly resembling those of a well-equilibrated melt, is again observed in the medium-range order. The data for the first coordination spheres of the models obtained via global optimizations and, to a lesser extent of those obtained via slow MC cooling, are similar to those in class A. Slower cooling leads to smaller deviations of the coordination numbers of silicon and boron from their ideal values four and three, respectively, and nitrogen atoms are always threefold coordinated and there is no preference for N-B coordination over N-Si coordination. However, the second coordination spheres reveal differences among the models and show the dependence of the structural properties on the thermal history. We find a decrease of the number of Si-Si and B-B next nearest neighbors with decreasing cooling rates γ for all models that were heated to temperatures $T \geqslant 2000$ K. For the slowest cooling rates (procedures 5 and 6), we also note that these coordination numbers of the second coordination

spheres approach the values found for the models determined from melt processing. This approach to the values of class A models is not found for the models, that were only heated to 1000 K initially or were cooled very fast from 2000 K.

The analysis of the ring statistics again shows the (dis) similarities to the models obtained from the melt procedure. Fast cooling leads to a higher fraction of four-member rings in all models, regardless of their thermal treatment. The differences between the models become clearer, if we focus on the fraction of six-member rings. The fraction of six-member rings decreases from a high value of about 40% to values of about 25% with a concomitant reduction in the relative amount of Si_3N_3 and B_3N_3 rings, once we heat the system to temperatures above 2000 K and keep it at that temperature for a sufficiently long time. Furthermore, the breakdown of "ring-ordering" is closely correlated with an increase in the number of Si-B next nearest neigbors.

3. Cluster models

For the cluster models, we find the same peaks in the pair correlation function as in the models derived from the melt-cooling procedures and the crystal fragment models. However, the first two peaks at 1.43 and 1.72 Å in the pair correlation function of the open cluster models, are substantially broader than the ones found for the periodically repeated interior of the cluster because of surface effects. Regarding the choice of the initial temperatures, the second double peak in the pair correlation functions of the open cluster models are more blurred than the corresponding peaks in the periodically repeated interior of the cluster. For the latter models, the splitting of the second double peak is much more pronounced, for slower cooling rates.

The dependence of the structural properties of the models on the process parameters is similar to the one for the crystal fragment models. Silicon atoms are mainly tetrahedrally coordinated by nitrogen, and boron and nitrogen atoms are mainly trigonally planar coordinated by nitrogen, and silicon or boron, respectively. Slower cooling leads to an increased coordination number of silicon and faster cooling leads to more BN_4 units. The second coordination spheres of the cluster-based models only show a weak preference for a high number of Si-Si and B-B next nearest neighbors over Si-B and B-Si next nearest neighbors. The relatively high number of Si-Si next-nearest neighbor contacts decreases, however, if the system is equilibrated at $T \geqslant 1500$ K for open boundary conditions and at $T = 2500$ K for periodic boundary conditions.

4. Class E: Sol-gel models

For the sol-gel models, we observe effects of the choice of the interaction potential in the intensity of the peak at about 2.45 Å of the second double peak in the pair correlation functions. However the pair correlation functions of the RMC-refined models are barely distinguishable from each other and agree with the experimental data fairly well (cf. Fig. 2). Note also that the number of initial aggregation sites does not influence the pair correlation function.

Before the annealing step, these models show a significant percentage of SiN_3 and BN_4 building units, resulting in rather low silicon mean coordination numbers and rather high boron coordination numbers compared to the experimental data, but this changes to the standard values after tempering. The second coordination sphere of these models shows a high number of B-B and Si-Si next nearest neighbors. This is an effect of the kinetic factor $p^0_{(\mathrm{N\text{-}B})} = 0.99$, which incorporates a higher bonding probability of free nitrogen atoms to boron than to silicon atoms. The high number of like cation next nearest neighbors is preserved, if we relax these sol-gel models via *NpT*-MC simulations at temperatures below 1000 K. In contrast, annealing at T

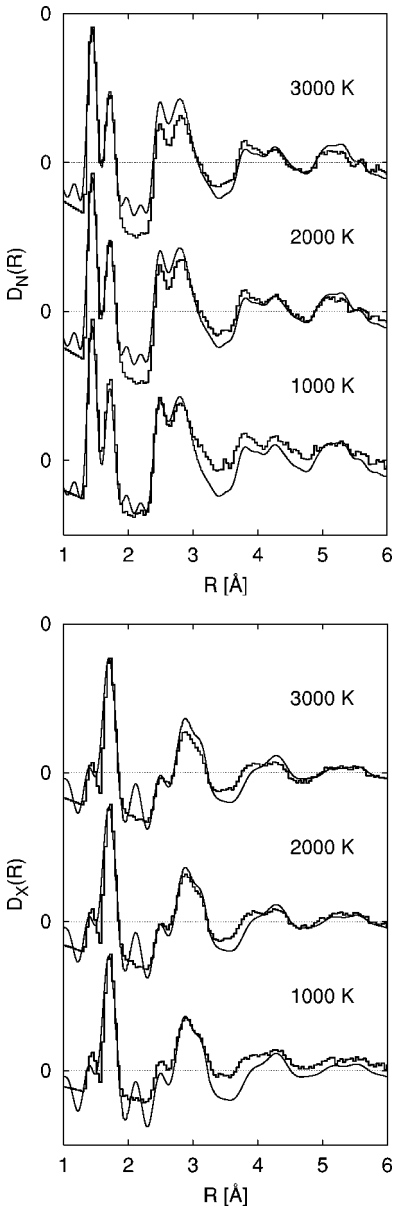

FIG. 2. Neutron (left) and x-ray (right) pair correlation functions for class E (sol-gel models) after final refinement, for three different relaxation temperatures. The data are for runs with 3 initial atoms placed on the lattice. The thin lines are the experimental data, where the small peaks up to 2.3 Å are artifacts of the measurement and analysis process (ghost peaks). Curves are shifted for clarity.

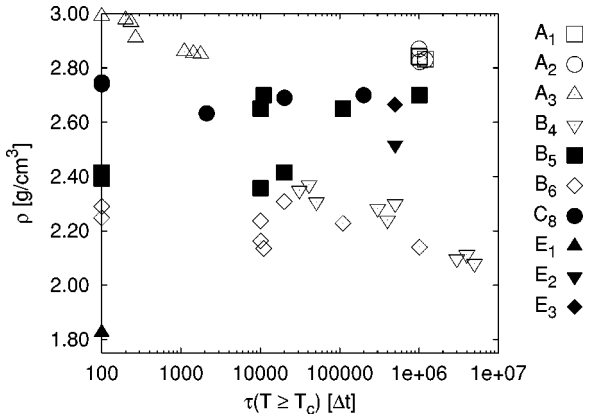

FIG. 3. Dependence of the densities of the locally optimized models on the time spent at temperatures above $T_c = 2000$ K during the cooling/optimization stage. Empty symbols denote (*NVT*)- and full symbols (*NpT*)-simulations, respectively. Δt is given in MCC for MC simulations, and fs for MD simulations, respectively.

$\geqslant 2000$ K leads to a strong compactification and the resulting final structures resemble those of the melt-based models.

IV. BULK PROPERTIES

A. Density

As is well known from models for other amorphous compounds forming covalent networks such as a-SiO_2, one of the most difficult quantities to model is the overall density.[21,22] The reason for this can be found both in the intrinsic faults of the models regarding structure design and energy function employed, and in the hidden features of the experimental structure in the nearly "inaccessible" range of 1/2–2 nm, which cannot be taken into account during the modeling process. On this length scale, we are usually not able to determine from the experimental measurements, whether a "dense" packing of the building units (tetrahedra, octahedra, etc.) is present, or whether small voids exist that are stable within the macroscopic real compound. Typically, these would not appear in the context of a high-temperature MD/MC simulation or any other modeling procedure that explicitly aims at generating the microscopic structure of the dense portion of the amorphous material.

Figure 3 shows the densities calculated for the various models. Again, we find that the closest agreement with experiment is found for the crystal fragment model (class B) and the sol-gel model (class E). However, in all cases, the void-free regions show a density of $\rho^{\text{dense}} \approx 2.5-2.8$ g/cm^3. This should be compared with the density of hypothetical crystalline ternary compounds ($\rho^{\text{cryst}} \approx 2.9$ g/cm^3),[9] and the appropriate weighted average of the experimental densities of crystalline BN and Si_3N_4 ($\rho^{\text{aver}} \approx 2.75$ g/cm^3). This suggests that the reason for the surprisingly low density of a-$Si_3B_3N_7$ might be the existence of stable voids with diameters below 1 nm, which would be difficult to determine experimentally.

Since the synthesis route via the sol-gel process would naively be expected to lead to many mismatches and the formation of cavities of all sizes, the fact that the final density of the sol-gel model agrees best with experiment appears to be self-consistent, and justifies faith in the model generating procedure. However, the data depicted in Fig. 3 shows a wide spread even for a single model class. Thus we first discuss the dependence of the densities of the models on the process parameters employed in their generation, and later comment on the influence of voids.

Regarding the dependence of the densities of the various models on the cooling rates γ^A_{NVT} and γ^A_{NPT} after constant pressure local optimizations, we find a decrease of the final densities after slower cooling during the *NVT*-stage of the simulations. No difference between, e.g., the melt-based MD models (A_1) and the melt-based MC models (A_2) is observable. The *NVT* cooling simulations relieve the strain in the system, and the final constant pressure local optimizations bring the system to the closest minimum with respect to both atomic positions and cell parameters, thereby not changing the densities dramatically. Similarly, potential effects are most pronounced if the system has been cooled rapidly, thus leaving the system in a highly strained state, where details of the local optimizations can be important.

The *NpT* cooling procedure shows, that slower cooling leads to higher densities of the final structural models after local optimization. However, the densities of sol-gel and crystal-fragment models change by about 50% after heating above 2000 K and do not only depend on the choice of the cooling rates, but also on the choice of the initial temperatures T_0, that were used in the *NpT*-cooling simulation. The densities of the models that were cooled very rapidly ($\gamma = 0.1$ K/MCC) are rather low (≈ 2.3 g/cm^3, approximately equal to the densities of the *NVT* cooled models). But for slower cooling the densities of the crystal fragment-based models reach the densities of the melt-based models, provided that the system had been heated to at least 2000 K, no matter, whether we performed the local optimization in two steps (constant volume followed by constant pressure local optimizations) or directly under constant pressure conditions. The reason for the dramatic change in the density of crystal fragment models can be found in the structural freezing-in of the system at temperatures below 2000 K.[23,24] For $T \leqslant 2000$ K, the changes in densities become very small, and also for rapid cooling (10^{-1} K/MCC) lower densities result, since the time spent above 2000 K is very short.

Finally, we note, that quite generally, the higher density models are energetically more favorable than the low-density models. This is consistent with the overall tendency to densification once the temperatures are high enough. (A more detailed analysis of these processes for $T < 2000$ K is presented elsewhere.[25])

B. Phonon densities of states and bulk moduli

We used the GULP-program[26] for the calculation of the phonon density of states V DOS(ν) and the bulk moduli B. These properties were determined for all models after employing the four local optimization strategies. Figure 4 shows the bulk moduli as a function of the excess energy $\Delta E_{A/B} = E^{A/B}_{\text{amorph}} - E^{A/B}_{\text{cryst}}$, for the two interaction potentials A and B,

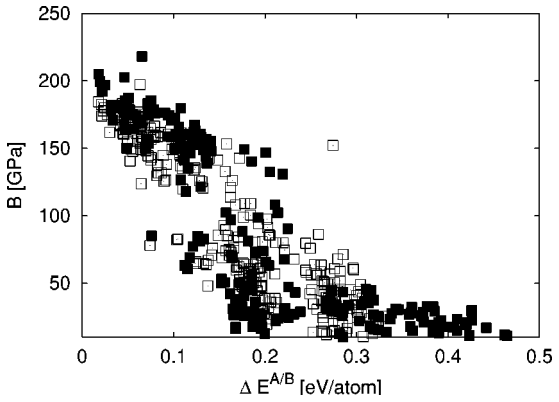

FIG. 4. Dependence of the bulk moduli B (in GPa) on the excess energies $\Delta E_{A/B}$ (in eV/atom). The data calculated with potential A and B are shown as filled and open symbols, respectively.

for all of the about 500 local minima that occurred in the study of the different models of classes A–E using potentials A and B, respectively. $E_{\mathrm{cryst}}^{A/B}$ are the potential energies of a hypothetical crystalline polymorph[27] for $Si_3B_3N_7$. We find a distinct correlation between the potential energy and the elastic strength of the material. The lower the energy of the amorphous structure, the higher is the bulk modulus. Except for the high-lying minima, the values of the bulk moduli of the investigated systems depend very little on the choice of the interaction potential. Similarly, the denser the system, the higher is its bulk modulus, and again the results do not depend on the choice of the interaction potential.

Finally, Fig. 5 shows the phonon densities of states calculated as averages over all structures found for each class, employing interaction potentials A and B in the local optimization and the subsequent matrix diagonalization. The overall shapes of the *V* DOS are the same, with only slight differences in the high-frequency regions, where the peak at about 1500 cm^{-1} is less pronounced for the models of classes B and E. Comparison with the calculated phonon densities of states of crystalline β-Si_3N_4 and hexagonal boron nitride shows that the peak at 1500 cm^{-1} can be associated with vibrations of hexagonal BN, while the peaks at about 1000 cm^{-1} are mostly associated with Si-N lattice vibrations. (A more detailed discussion of the vibrational properties and their relation to the dynamics in $Si_3B_3N_7$ is presented elsewhere.[28]) The choice of interaction potential does not change the phonon densities of states significantly; only the intensities of the peaks in the phonon spectra of the crystal-fragment models depend on the choice of the interaction potential.

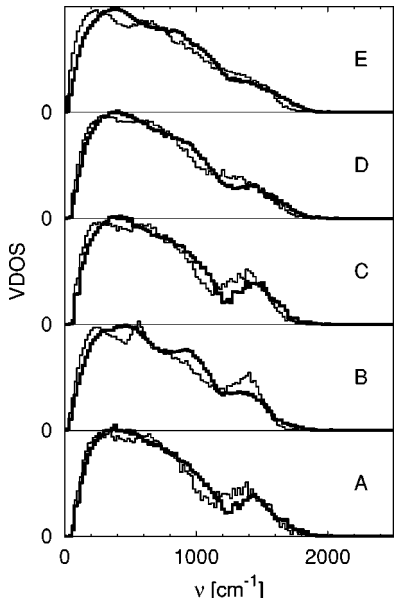

FIG. 5. Phonon spectra of models representing the classes A–E. Thin lines denote the phonon densities of states calculated after local optimizations using potential A and bold lines represent data after local optimizations using potential B.

V. DISCUSSION

In all structural models boron and silicon atoms are mainly trigonally planar and tetrahedrally surrounded by three and four nitrogen nearest neighbors, respectively, and nitrogen atoms are surrounded by three cations (silicon or boron atoms). These results agree well with the experimental investigations of *a*-$Si_3B_3N_7$. Independent of the model classes, we found that faster cooling leads to more coordination defects, i.e., deviations from the ideal coordination numbers four, three and three of silicon, boron and nitrogen atoms, respectively. The RCP-based models were only quenched (viz., infinitely fast cooling) and showed the highest number of coordination defects. These results confirm the general observation in our studies, that faster cooling leads to more coordination defects. (The choice of the interaction potential affected the properties of only those models, that had been very rapidly quenched. But the general dependence on the cooling rates was not affected by either the choice of the interaction potential or the local optimization strategy employed.) Vollmayr *et al.* found similar cooling rate dependences in their study of the structural properties of *a*-SiO_2.[21] Note, however, that in the *a*-$Si_3B_3N_7$ system two cationic atoms exist that show a different relative number of coordination defects. These defects are more pronounced for silicon than for boron atoms, clearly showing that nitrogen atoms are more tightly bound to boron than to silicon atoms.

Even though the first coordination spheres of the atoms were almost identical for all models, significant differences were found in the second coordination spheres of the models. The melt-, cluster- and RCP-based models showed rather homogeneous distributions regarding the type of cations surrounding a given cation in the second coordination sphere. In contrast, the crystal fragment- and sol-gel-based models showed a preference for boron/silicon atoms surrounding a given boron/silicon atom, respectively, in the second coordination sphere. However, for both the sol-gel and the crystal-fragment-based models, the heterogeneous distributions of cations disappeared once the system had been heated above 2000 K for a sufficiently long time. (Note, that these results did not depend on the local optimization strategy employed, nor on the choice of interaction potential used in the local optimization.)

The x-ray and neutron pair correlation functions of the crystal-fragment- and the sol-gel-based models showed good

agreement with the experimental data as long as the system was kept below 2000 K. In contrast, the pair correlation functions of models in classes A, C, and D, fit the experimental data (at 298 K) only moderately well, with a nearly total lack of features at distances $R > 3.5$ Å. Such features beyond 3.5 Å are present in the pair correlation functions of the crystal fragment- and the sol-gel-models, but they vanish as the heterogeneous distribution of cations disappears upon heating to temperatures $T > T_C$.

All model structures are essentially compact, and no large rings containing more than 16 atoms are found. We did not find significant cooling rate effects in the overall distribution of ring sizes; only an increase of four-member rings in the models obtained after very fast cooling was detectable. These trends in the ring statistics are similar to results of Vollmayr *et al.*[21] for the *a*-SiO_2 system. The crystal fragment-based model is distinctive in that it exhibits a ring distribution with a strong preference for six-member Si_3N_3 and B_3N_3 rings. Models in classes A, C, and D contain much fewer six-member rings mostly showing mixed cation content, while the sol-gel-based models are in-between the crystal fragment- and the melt-based models. However, once the crystal fragment models had been heated above 2000 K, the ring distribution changed to the one found for class A.

The models belonging to the various classes exhibit different densities, ranging from 1.8 g/cm^3 to 2.9 g/cm^3, where the ones of the crystal fragment- and sol-gel-based models are closest to the experimental densities. The densities of the models belonging to the other classes are all larger than 2.6 g/cm^3, indicating that the synthesis route is important for the final density of the "product." In agreement with our earlier considerations, the crystal fragment- and sol-gel-based models showed a considerable increase in the density once these models experienced prolonged heating at temperatures above 2000 K.

One of the most fascinating outcomes of this comparison of five different synthesis routes is that the differences between the model classes regarding their medium range order are larger than the variations within a class (cf. Table V). This is most noticeable in the density or bulk modulus, but also in, e.g., the neutron and x-ray pair correlation functions, or the coordination numbers. Clearly, this should carry over to the experiment: different synthesis routes should result in different amorphous "structures" with different structural and physical properties.

To summarize, the crystal fragment- and the sol-gel based models are in good agreement with all experimental data, thus indicating that the microscopic structure of the real *a*-$Si_3B_3N_7$ material is close to these models.

Finally, we would like to comment on cooling rate effects and on the influence of the simulation method employed on the outcome of our investigations. Regarding the energies of the models, we found that the dense models belonging to classes A and C are energetically more stable than the low-density models in classes B and E. A seeming exception of this rule were the dense RCP-based models. However, due to the lack of an explicit tempering stage, these structures exhibited a relatively large number of coordination defects, leading to somewhat higher energies than those for structures in classes A and C.

Even though the magnitudes of the densities were specific for one model class, the cooling rate dependence of the densities was rather general. For the *NVT*-simulations, we found that slow cooling (cf. Fig. 3) led to lower densities of the locally optimized models, regardless of the strategy employed in the final local optimizations. Since cooling in the *NVT*-ensemble relieved the strain at constant (relatively large) volume, slower cooling resulted in smaller final strain, and thus the final constant pressure local optimization did not shrink the cell volume by a large amount. In contrast, cooling in the *NpT*-ensemble led to higher densities of the models for slower cooling. (Note, that we did not find any difference between MC and MD cooling simulations.)

Our observations regarding cooling rate effects are in good agreement with simulations and experiments for other simpler systems. For *a*-SiO_2, Vollmayr *et al.*[21] found a decrease of the density with increasing cooling rate in a MD-*NpT* computer simulation study, but the authors pointed out that these results may be due to the density anomaly of *a*-SiO_2. In a study on binary Lennard-Jones glasses, the same authors[29] found that the density increases with decreasing cooling rates. Furthermore, the density of borosilicate glasses increases upon slower cooling in experiments.[30,31]

The dependence of the energies on the cooling rates was independent of the investigated model class and ensemble used in the simulation, where slower cooling led to lower energies. Similar cooling rates effects on the energy distribution have also been found in computer simulations of spin glasses,[32] hard optimization problems,[33] *a*-SiO_2,[21] and Lennard-Jones glasses,[29] just to name a few of the complex systems investigated.

Based on the energies of the structures, both the sol-gel- and the crystal fragment-based models are only metastable with respect to the melt-based models. This is reflected in the structural changes we observe when heating the models above $T_c = 2000$ K for a sufficiently long time. However, at low temperatures (i.e., below 2000 K), the time scales of neither the experiment nor our simulations (the time scales of our simulations are $\approx 1-5$ ns, and are thus short compared to experimental time scales. Nevertheless, even increasing the length of the simulations by an order of magnitude did not lead to significant changes since, below 2000 K, the system remains essentially trapped inside regions of structurally similar minima) are long enough to transform the system to one of its low energy-high density amorphous configurations [of course, even low energy/high density models of amorphous structures are only metastable against crystallization (to crystalline $Si_3B_3N_7$) and phase separation (into crystalline BN and Si_3N_4) at infinite simulation times[12]] which are structurally different from the initial low density structures.

Based on these studies, we suggest that the low density of the amorphous compounds observed experimentally can be explained by the presence of nano-sized voids ($\oslash < 1$ nm) in the structure. (A more detailed analysis of the nano-sized voids will be presented elsewhere.[25]) Our simulations of the sol-gel route show, that such voids are generic to this process. This void-based explanation of the low-density of *a*-$Si_3B_3N_7$ is also supported by recent experimental results of Sauter *et al.*[34] of the vacancy sizes in amorphous B-C-N ceramics. One should also note, that our simulations actually

underestimate the stability of voids. In the experiments a dense crust will form at the surface of the material once all the voids near the surface have been expelled. Thus the densification of the ceramic is strongly inhibited. In contrast, voids can be rather easily removed in a simulation with periodic boundary conditions—the effective surface is only a few nanometers away.

Finally, we note that, similar to the results of Omeltschenko *et al.*[35] on low density amorphous Si_3N_4, the bulk moduli of the *a*-$Si_3B_3N_7$ models decreased with decreasing density of the models. Furthermore our results support Stillinger's view,[36] that the bulk modulus of an amorphous material depends on the height of the minimum on the energy landscape, in the sense that the low-lying minima have steeper walls than the high-lying minima.

VI. SUMMARY AND CONCLUSION

We have shown that the properties of the amorphous ceramic *a*-$Si_3B_3N_7$ strongly depend on the way we generate models belonging to different classes of synthesis routes on the computer. The models that contain a certain degree of heterogeneity in the second coordination sphere agree well with the experimental pair correlation functions, the experimentally determined first and second coordination spheres, and the experimental densities. The unusually low density of *a*-$Si_3B_3N_7$ is most probably due to the existence of subnanometer sized voids. Our results also show, that the amorphous ceramics produced via the sol-gel route are less dense, and probably energetically less stable, than those one might be able to synthesize in the future via, e.g., the glass formation route. Nevertheless for application temperatures below $T_C \approx 2000$ K, the present ceramic should prove to be sufficiently stable for long-time applications.

The great variety in the structures resulting from the various modeling approaches shows that at least some aspects of the particular synthesis route need to be included in future modeling strategies for these new types of amorphous compounds. Finally, we would like to point to the plethora of rather different and experimentally distinguishable amorphous structures that we expect will be found when following different synthesis routes in actual experiments. While these might be difficult to perform for the amorphous nitrides, a similar variety of different amorphous "structures" should also occur in other complex amorphous systems such as multinary amorphous oxides, which might be more easily accessible experimentally.

ACKNOWLEDGMENTS

We would like to thank C. Oligschleger and S. Wefing for valuable discussions. Funding was kindly provided by the DFG via SFB408.

[1] H. P. Baldus, O. Wagner, and M. Jansen, in *Materials Research Society Symposium Proceedings*, edited by M. J. Hampden-Smith, W. G. Klemperer, and C. J. Brinker (Materials Research Society, Warrendale, 1992), Vol. 271, pp. 821–826.
[2] M. Jansen and P. Baldus, Angew. Chem., Int. Ed. Engl. **36**, 328 (1997).
[3] P. Baldus, M. Jansen, and D. Sporn, Science **285**, 699 (1999).
[4] A. Hannemann, J. C. Schön, C. Oligschleger, and M. Jansen, in *Proceedings of DGK-Workshop on "Struktur und Eigenschaften Nichtkristalliner Materialien—Meßdaten und Strukturmodelle"* (Wolfersdorf Sept. 1999), edited by B. Müller (University of Jena, Jena, 1999); also as cond-mat/000131 (unpublished).
[5] U. Müller, W. Hoffbauer, and M. Jansen, Chem. Mater. **12**, 2341 (2000).
[6] D. Heinemann, W. Assenmacher, W. Mader, M. Kroschel, and M. Jansen, J. Mater. Res. **14**, 3746 (1999).
[7] L. van Wüllen, U. Müller, and M. Jansen, Chem. Mater. **12**, 2347 (2000).
[8] L. van Wüllen, U. Müller, and M. Jansen, Angew. Chem., Int. Ed. **39**, 2519 (2000).
[9] P. Kroll and R. Hoffmann, Angew. Chem., Int. Ed. **37**, 2527 (1998).
[10] M. Allen and D. Tildesley, *Computer Simulations of Liquids* (Clarendon, Oxford, 1987).
[11] M. Gastreich, C. Marian, and J. Gale, Phys. Rev. B **62**, 3117 (2000).
[12] A. Hannemann, J. C. Schön, and M. Jansen (unpublished).
[13] R. Bell and P. Dean, Philos. Mag. **25**, 1381 (1972).
[14] L. Gladden, J. Non-Cryst. Solids **119**, 318 (1990).
[15] S. Wefing, J. Non-Cryst. Solids **244**, 89 (1999).
[16] A. Hannemann, J. C. Schön, and M. Jansen, Comput. Phys. Commun. **144**, 284 (2002).
[17] J. C. Schön, A. Hannemann, and M. Jansen, J. Phys. Chem. B **108**, 2210 (2004).
[18] T. Jäschke, Ph.D. thesis, Universität Bonn, Shaker Verlag, Aachen, 2002.
[19] M. Gastreich, J. Gale, and C. M. Marian, in *Physics of Glasses: Structure and Dynamics*, edited by P. Jund and R. Julien (AIP, New York, 1999), Vol. 489, AIP Conf. Proc., pp. 237–242.
[20] R. Hagenmayer, U. Müller, C. J. Benmore, J. Neuefeind, and M. Jansen, J. Mater. Chem. **9**, 2865 (1999).
[21] K. Vollmayr, W. Kob, and K. Binder, Phys. Rev. B **54**, 15808 (1996).
[22] K. Binder, Comput. Phys. Commun. **122**, 168 (1999).
[23] A. Hannemann, J. C. Schön, M. Jansen, and P. Sibani (unpublished); also as cond-mat/0212245 (2002).
[24] J. C. Schön, A. Hannemann, G. Sethi, M. Jansen, P. Salamon, R. Frost, and L. Kjeldgaard, in *XXIII DGK-Workshop on Structure and Kinetics of Nucleation and Crystallization in Non-crystalline Materials*, edited by B. Müller (University of Jena, Jena, 2002), also as cond-mat/0212279.
[25] A. Hannemann, J. C. Schön, and M. Jansen (unpublished).
[26] J. D. Gale, J. Chem. Soc., Faraday Trans. **93**, 629 (1997).
[27] J. C. Schön and M. Jansen, Angew. Chem., Int. Ed. Engl. **35**, 1286 (1996).
[28] A. Hannemann, J. C. Schön, and M. Jansen, in Proceedings of

DGK Workshop on "Strukturen und räumliche sowie zeitliche Strukturbildungsprozesse im intermediären Strukturbereich nichtkristalliner Materialien" (Wolfersdorf Sept. 2004), edited by B. Müller (Universitat Jena, Jena 2004, in press)..

[29] K. Vollmayr, W. Kob, and K. Binder, J. Chem. Phys. **105**, 4714 (1996).

[30] H. Lillie and H. Ritland, J. Am. Ceram. Soc. **37**, 466 (1956).

[31] H. E. Hagy and H. N. Ritland, J. Am. Ceram. Soc. **40**, 436 (1957).

[32] K. H. Fischer and J. A. Hertz, *Spin Glasses* (Cambridge University Press, Cambridge, 1991).

[33] P. Salamon, P. Sibani, and R. Frost, *Facts, Conjectures, and Improvements for Simulated Annealing* (SIAM Monographs, Philadelphia, 2002).

[34] D. Sauter, M. Weinmann, F. Berger, P. Lamparter, K. Müller, and F. Aldinger, Chem. Mater. **14**, 2859 (2002).

[35] A. Omeltschenko, A. Nakano, R. Kalia, and P. Vashishta, Europhys. Lett. **33**, 667 (1996).

[36] T. Weber and F. Stillinger, Phys. Rev. B **31**, 1954 (1985).